Weak Host Interactions Induced Thermal Transport Properties of Metal Halide Perovskites Deviating from the Rattling Model

Yu Wu,*,† Linxuan Ji,‡ Shuming Zeng,¶ Yimin Ding,† and Liujiang Zhou*,‡,†

† Yangtze Delta Region Institute (Huzhou), University of Electronic Science and Technology, Huzhou, Zhejiang 313001, China

‡School of Physics, State Key Laboratory of Electronic Thin Films and Integrated Devices,
University of Electronic Science and Technology, Sichuan, Chengdu 611731, China

¶College of Physics Science and Technology, Yangzhou University, Jiangsu 225009, China

E-mail: wuyu@csj.uestc.edu.cn; ljzhou@uestc.edu.cn

Abstract

The low-frequency phonon branches of metal halide perovskites typically exhibit the characteristic of hardening with the increase of the cation mass, which leads to anomalous thermal transport phenomenon. However, the underlying physical mechanism is not yet understood. Here, we theoretically compare the thermal transport properties of $A_2\mathrm{SnI}_6$ ($A=\mathrm{K}$, Rb, and Cs) perovskites. The thermal transport in perovskites is widely explained using the rattling model, where "guest" cations inside the metal halide framework act as "rattlers", but this fails to explain the following phenomenon: The low-frequency phonon branch of $A_2\mathrm{SnI}_6$ perovskites is insensitive to the mass of the A^+ cation and strongly correlated with the interaction of the A^+ cation with the I⁻ anion in the octahedral structures. The failure of the rattling model stems mainly from the weak interactions between the octahedral structures. And we find that this

weak interaction is prevalent in other metal halide perovskites. By developing a new spring model, we successfully explain the thermal transport behavior in A_2 SnI₆ perovskites. Our work gives new insights into the thermal transport mechanism in metal halide perovskites, which has a guiding significance for designing extremely low thermal conductivity materials.

Introduction

The metal halide perovskites are widely used in the field of photovoltaics, ^{1,2} light-emitting diodes, ^{3,4} photodetectors, ⁵⁻⁷ and thermoelectrics ^{8,9} owing to their excellent light absorption capability, the relatively long diffusion length of charge carriers and tunable bandgap. Understanding the heat transport mechanism of perovskites is essential for the thermal management of perovskite-based devices. On the one hand, devices such as photodetectors require materials with high thermal conductivity to provide heat dissipation and thus enhance operational lifetime. On the other hand, the thermoelectric field requires low lattice thermal conductivities for large energy conversion efficiencies.

The heat transport mechanism of perovskites is closely related to its special crystal structure. Take the common ABX_3 -type metal halide perovskites as an example, the framework is composed of corner-shared BX_3^- octahedra with metals (e.g., Pb^{2+} , Sn^{2+}) at the center and halide anions at the corners. The A-site cations (e.g., Cs^+ , organic cations) are located in the hollow within the perovskite framework. The soft phonon modes and large lattice anharmonicity results from the rattling motion of A-site cations and dynamic rotation of halide atoms have long been considered to be the key factors limiting lattice thermal transport of metal halide perovskites. $^{10-13}$ However, these theories cannot account for the following facts: 1) There is no distinct avoid-crossing phenomenon between the acoustic and optical branches, 8,14 which is a typical characteristic of the rattling model. $^{15-18}$ 2) As the mass of A-site cations increases, the low-frequency phonon branches harden, which further brings about anomalous mass-dependent thermal transport phenomenon. $^{19-22}$ Moreover, the

thermal transport of the CsPbI₃ and empty PbI₆ frameworks was compared and it was found that Cs⁺ cations lead to an enhancement in thermal conductivity. ²³ Therefore, exploring the effect of A-site cations and the failure of the rattling model is critical to understanding the thermal transport properties of metal halide perovskites.

Here, we studied the thermal transport properties of a class of vacancy-ordered metal halide perovskites $A_2\mathrm{SnI}_6$ ($A=\mathrm{K}$, Rb, and Cs). The structure can be regarded as a defect variant of $A\mathrm{SnI}_3$ with isolated $[\mathrm{SnI}_6]^{2-}$ octahedra bridged by A-site cations. The results show that Cs-based perovskites have greater A-I interactions. The low-frequency phonon branches are not sensitive to the mass of A-site cations and strongly correlate with the A-I interactions, which leads to a larger particlelike thermal conductivity of $\mathrm{Cs}_2\mathrm{SnI}_6$. The rattling model failure arises from weak interactions between the octahedra, which is inconsistent with the strong interaction condition of the host frame in the model. By building a spring model with weak host interaction, we successfully explain the anomalous thermal transport behavior of $A_2\mathrm{SnI}_6$. Further analysis shows that this weak interaction still exists even though the octahedral structure is corner-shared, making this anomalous behavior prevalent in metal halide perovskites.

Results and Discussion

The $A_2\mathrm{SnI}_6$ ($A=\mathrm{K}$, Rb, and Cs) perovskites have a face-centered cubic lattice with space group $Fm\overline{3}m$ and are typically described as $A_2^+\mathrm{Sn}^{4+}\mathrm{I}_6^-$. Each Sn^{4+} is bonded to six equivalent I⁻ to form an isolated $[\mathrm{SnI}_6]^{2-}$ octahedron, which is bridged by A^+ cations as shown in Fig. 1(a). The structure of $A_2\mathrm{SnI}_6$ perovskites differs from the host-guest system corresponding to the rattling model, where the adjacent atoms in the host have bonding connections. Specifically, the A^+ cations can be viewed as guest atoms, however, the $[\mathrm{SnI}_6]^{2-}$ octahedra cannot be viewed as host frames in the traditional sense due to the lack of strong bonding between them. Figure 1(b) shows the particlelike thermal conductivities (κ_p) of $A_2\mathrm{SnI}_6$ per-

ovskites at 300 K. $A_2\mathrm{SnI_6}$ perovskites exhibits anomalous mass-dependent κ_p . The Cs₂SnI₆ perovskite has the largest total atomic mass but exhibits the highest κ_p . Considering three-phonon (3ph) scattering, The κ_p of Cs₂SnI₆ is 17.2% higher than that of Rb₂SnI₆. When four-phonon (4ph) scattering is introduced, the difference between κ_p is further amplified to 72.7%. The glasslike thermal conductivity (κ_c) contributed by wavelike phonon tunneling in $A_2\mathrm{SnI_6}$ perovskites cannot be ignored as shown in Fig. 1(c). Taking Cs₂SnI₆ as an example, κ_c occupies 28.0% of the total thermal conductivity ($\kappa_L = \kappa_p + \kappa_c$). The κ_c of $A_2\mathrm{SnI_6}$ perovskites exhibits two distinctive features: 1) It shows a gradual decrease with total atomic mass. 2) Considering 3+4ph scattering, κ_c is significantly improved compared to the result when considering only 3ph scattering. κ_c is closely related to phonon lifetime, and low lifetime phonons will contribute more to κ_c . ^{11,24–27}

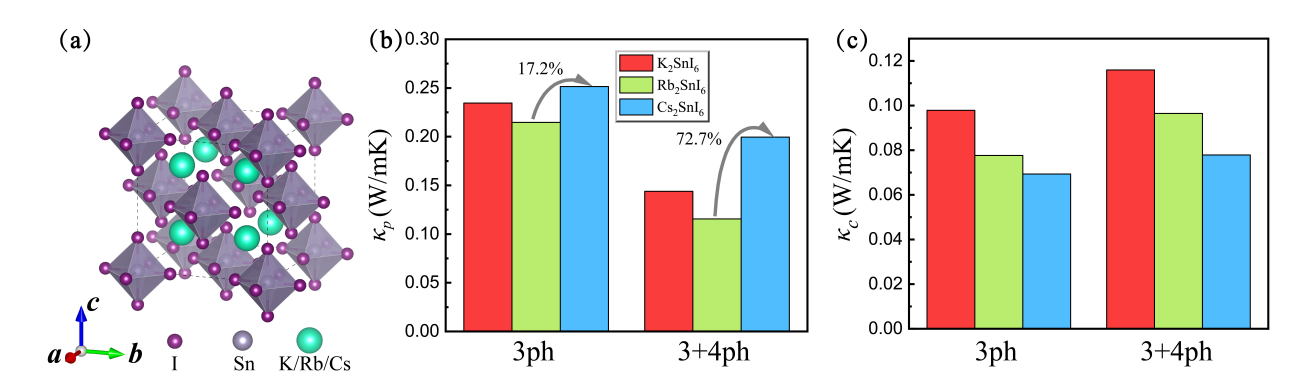


Figure 1: (a) The conventional cell of $A_2 \text{SnI}_6$ perovskites. (b) The particlelike thermal conductivities (κ_p) of $A_2 \text{SnI}_6$ perovskites at 300 K. (c) The glasslike thermal conductivities (κ_c) of $A_2 \text{SnI}_6$ perovskites at 300 K.

Figure 2(a-c) shows the phonon dispersion projected by the eigenvectors of each atom. The low-frequency (<1 THz) phonon branches are mainly contributed by the I⁻ in the octahedral structure. From K_2SnI_6 to Cs_2SnI_6 , the low-frequency phonon branches gradually harden. Especially for Cs_2SnI_6 , the frequency of the first optical branch at Γ point is 3.6 times that of Rb_2SnI_6 . The A^+ cations mainly contribute to optical branches in the range of 1 to 1.5 THz in A_2SnI_6 . It is noted that there is a clear boundary between the optical branches contributed by the A^+ cations and the acoustic branches, which is inconsistent with

the characterization of the rattling atom. In the classical rattling model, the low-frequency optical phonons contributed by guest atoms and the acoustic phonons are coupled together and induce the avoid-crossing feature of phonon dispersion. To investigate the effect of the atomic mass of the A-site on the thermal transport of A_2 SnI₆ perovskites, Fig. 2(d) shows the change of κ_p after modifying the atomic mass of Cs in Cs₂SnI₆. Replacing the mass of Cs with K and Rb in Cs₂SnI₆ results in a further increase in κ_p . The phonon dispersion of the original Cs₂SnI₆ and the phonon dispersion after replacing the Cs mass with the Rb mass are shown in Fig. 2(e). The A-site atomic mass has a negligible effect on the low-frequency phonon branch at frequencies smaller than 1 THz, and the decrease in the A-site atomic mass causes the optical branch it contributes to move toward higher frequencies. This further reduces the scattering channels of acoustic phonons as can be seen from the weighted 3ph scattering phase space (WP₃) in Fig. 2(f). The dependence of the phonon dispersion on A^+ mass is markedly different from the typical material YbFe₄Sb₁₂ for which the rattling model applies as seen in Fig. S1.

To understand the origin of the κ_p enhancement of $\mathrm{Cs_2SnI_6}$ perovskite, we examined the individual contributions of the heat capacity C_v , group velocity v_g , and phonon lifetime τ by replacing mode-resolved C_v , v_g , and τ of $\mathrm{Cs_2SnI_6}$ independently with those of $\mathrm{Rb_2SnI_6}$. Replacing C_v and v_g has a negligible effect on κ_p . In contrast, the κ_p drops dramatically after the replacement τ , which is close to the result of $\mathrm{Rb_2SnI_6}$. The τ is closely related to the scattering induced by phonon-phonon interactions, and the scattering strength and the scattering channels determine its magnitude. The scattering strength is related to the lattice anharmonicity, which can be reflected by the Grüneisen parameter γ . Figure 3(b, c) shows the phonon dispersion of $\mathrm{Rb_2SnI_6}$ and $\mathrm{Cs_2SnI_6}$ projected by $|\gamma|$. The $|\gamma|$ in $\mathrm{Rb_2SnI_6}$ is generally higher than that in $\mathrm{Cs_2SnI_6}$. At the Γ point, the $|\gamma|$ of the first optical branch in $\mathrm{Rb_2SnI_6}$ is an order of magnitude higher than that in $\mathrm{Cs_2SnI_6}$. The scattering channels can be reflected by weighted phase space. Figure 3(d, e) shows the 3ph (WP_3) and 4ph (WP_4) weighted phase space of $A_2\mathrm{SnI_6}$ perovskites, respectively. $\mathrm{Cs_2SnI_6}$ has significantly smaller

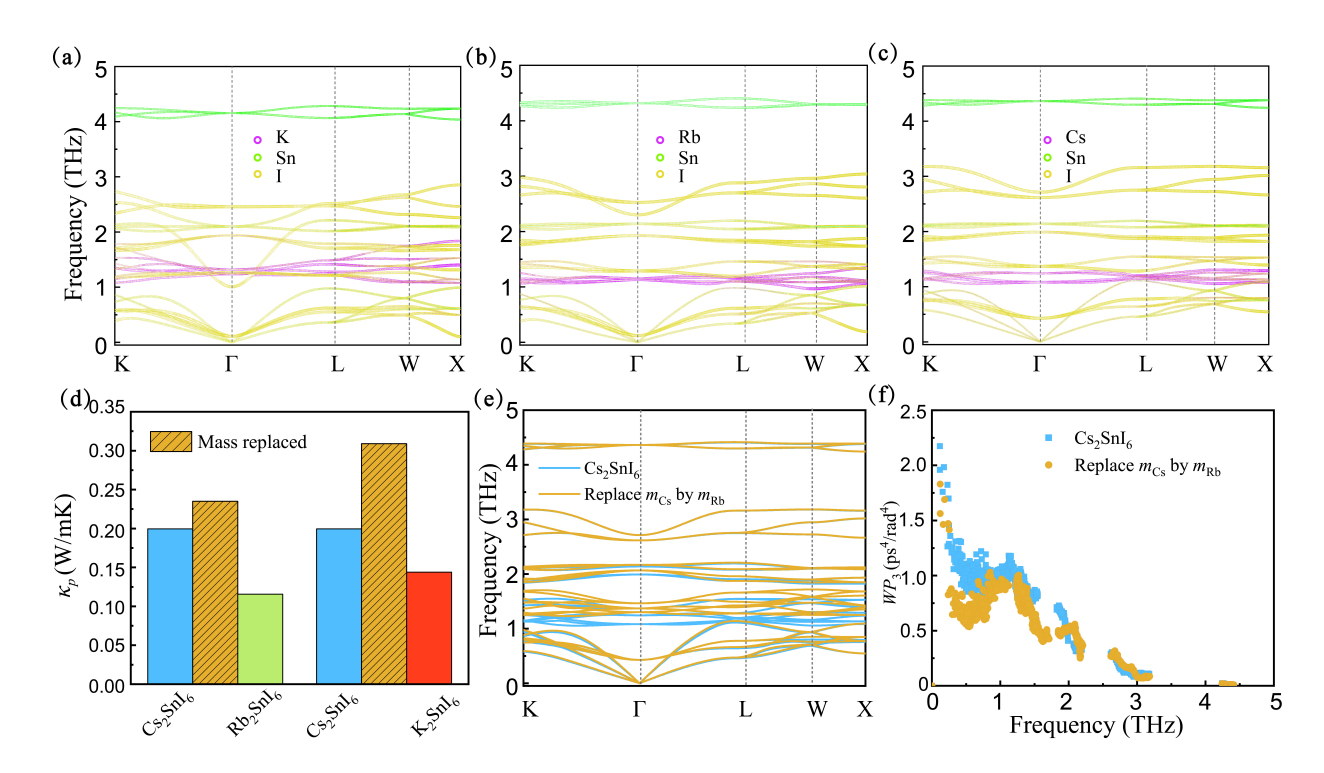


Figure 2: (a-c) The phonon dispersion projected by the eigenvectors of each atom in $A_2 \text{SnI}_6$ perovskites. (d) The κ_p after modifying the atomic mass of Cs in Cs₂SnI₆. (e) The phonon dispersion and (f) WP_3 of the original Cs₂SnI₆ and the phonon dispersion after replacing the Cs mass with the Rb mass.

3ph and 4ph scattering channels below 1 THz compared to K_2SnI_6 and Rb_2SnI_6 due to the hardening of low-frequency phonons, and phonons in this frequency range make a major contribution to κ_p as seen in Fig. S2. Figure 3(f) shows the phonon scattering rate, which is the reciprocal of the lifetime $(1/\tau)$. The weak phonon scattering strength and scattering channels in Cs_2SnI_6 make it the lowest scattering rate among the A_2SnI_6 perovskites.

To investigate the origin of the differences in the phonon lifetimes of $A_2\mathrm{SnI}_6$ perovskites, the norm of the second-order force constants $|\Phi_2|$ for the three strongest bonds are shown in the top of Fig. 4(a). The bottom shows the results with $|\Phi_2|$ in $\mathrm{K}_2\mathrm{SnI}_6$ being shifted to unity. In contrast to a relatively small increase for Sn-I and I-I bonds, the $|\Phi_2|$ of A-I bond in $\mathrm{Cs}_2\mathrm{SnI}_6$ increase by 28.9% compared with $\mathrm{Rb}_2\mathrm{SnI}_6$. Figure 4(b) shows the phonon dispersion of $\mathrm{Cs}_2\mathrm{SnI}_6$ and that after replacing $|\Phi_2(\mathrm{Cs}-\mathrm{I})|$ by $|\Phi_2(\mathrm{Rb}-\mathrm{I})|$. Significant softening of the low-frequency phonon branches occurs after modification of the $|\Phi_2|$, approaching the results

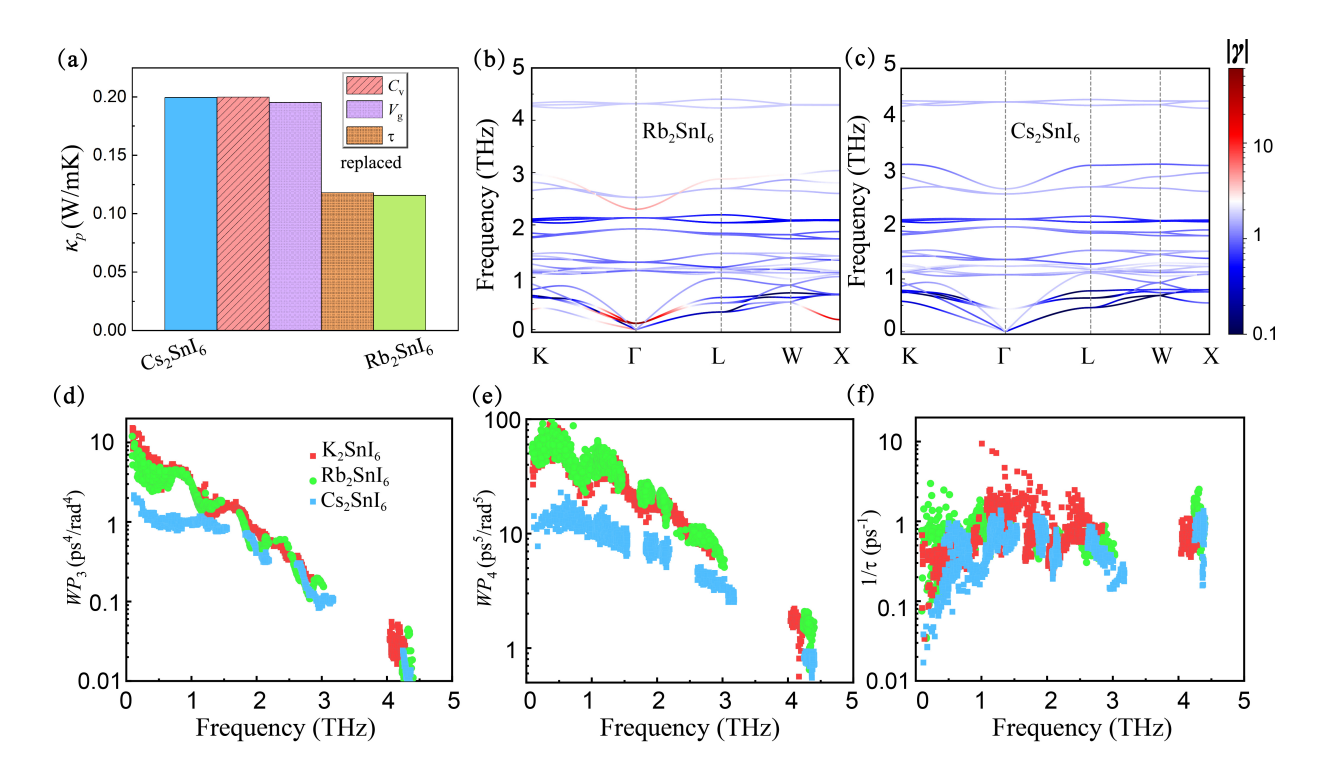


Figure 3: (a) The calculated κ_p at 300 K and the cross-calculated κ_p with the independent replacement of heat capacity, group velocity, and phonon lifetime. The phonon dispersion of (b) Rb₂SnI₆ and (c) Cs₂SnI₆ projected by $|\gamma|$. (d) 3ph and (e) 4ph weighted phase space of A_2 SnI₆ perovskites. (f) The scattering rates of A_2 SnI₆ perovskites.

of Rb₂SnI₆. The change in $|\Phi_2|$ can be related to the electronic bonding via the integrated crystal orbital Hamiltonian population (ICOHP). ²⁹ As seen in Fig. 4(c), the |ICOHP| value at the Fermi level for A-I bond matches the trend of the corresponding $|\Phi_2|$. At the same time, the strong A-I bond increases the rigidity of the material which the shear modulus can reflect. Further, it can be seen in Fig. 4(d) that the strong A-I bond in Cs₂SnI₆ greatly weakens the mean square displacements (MSD) of the Cs and I atoms.

The above discussion reveals an important feature of the thermal transport of $A_2\mathrm{SnI}_6$ perovskites: The low-frequency phonon branches, which are mainly contributed by the $[\mathrm{SnI}_6]^{2-}$ octahedra, are not sensitive to the mass of A^+ cations, but are sensitive to the interaction between A^+ and I^- in $[\mathrm{SnI}_6]^{2-}$ octahedra. Moreover, the disappearing avoid-crossing phenomenon of phonon dispersion suggests that the classical rattling model cannot explain the thermal transport properties. Based on the characterization of the weak interaction of

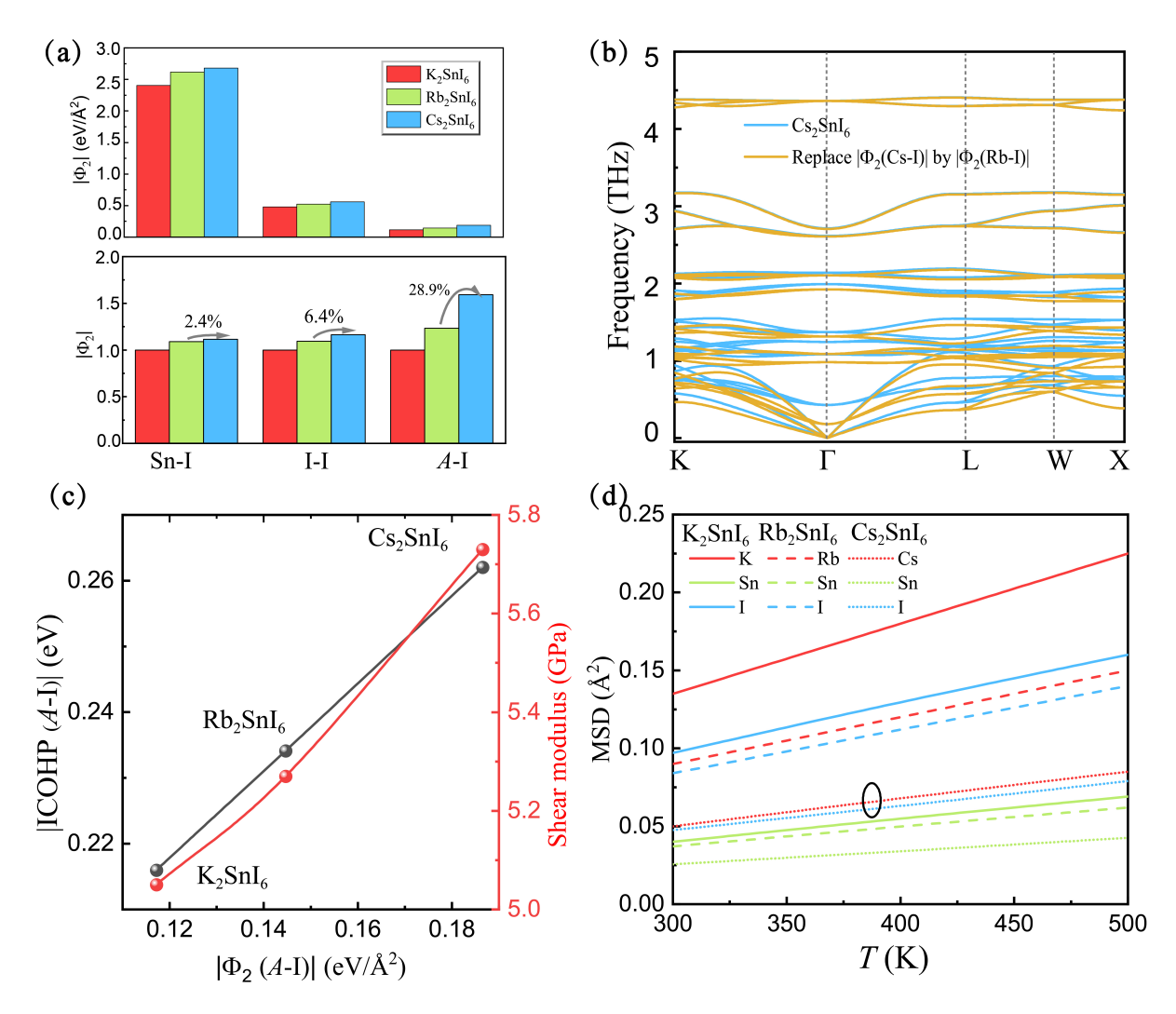


Figure 4: (a) The norm of the second-order force constants $|\Phi_2|$ for the three strongest bonds in $A_2\mathrm{SnI}_6$ perovskites. The bottom shows the results with $|\Phi_2|$ in $\mathrm{K}_2\mathrm{SnI}_6$ being shifted to unity. (b) The phonon dispersion of $\mathrm{Cs}_2\mathrm{SnI}_6$ and that after replacing $|\Phi_2(\mathrm{Cs}-\mathrm{I})|$ by $|\Phi_2(\mathrm{Rb}-\mathrm{I})|$. (c) The |ICOHP| value at the Fermi level and shear modulus as a function of the $|\Phi_2|$. (d) Calculated temperature-dependent atomic mean square displacements (MSD) of $A_2\mathrm{SnI}_6$ perovskites.

the octahedra in $A_2\mathrm{SnI}_6$ perovskites, we developed a spring model applicable to its thermal transport. As seen in Fig. 5(a), compared to the classical rattling model, ¹⁵ this model has a weak elastic constant K_1 between host frames. Figure 5(b) illustrates the structural units in the $A_2\mathrm{SnI}_6$ perovskites that coincide with the established spring models. The mass of atom A is m. See $[\mathrm{SnI}_6]^{2-}$ as a whole, where the sum of the mass of all atoms is M. The elastic constants K_1 and K_2 are determined by the Φ_2 between atoms. The parameters used in the

spring model are shown in Table S1. Figure 5(c) shows the analytical solution of the spring model corresponding to Cs_2SnI_6 . The acoustic branch frequency maximum and the optical branch frequency minimum are defined as ω_{a-max} and ω_{o-min} , respectively. Figures 5(d, e) give the variation of ω_{a-max} and ω_{o-min} after varying m as well as K_2 on the basis of the Cs_2SnI_6 spring model parameters, respectively. ω_{a-max} is insensitive to changes in m, and the gradual increase with K_2 is consistent with the rule demonstrated in Fig. 2(e) and Fig. 4(b). To investigate the effect of K_1 on phonon dispersion, Fig. S3(a) shows the solution of the spring model of Cs_2SnI_6 with 5 times the original K_1 . The avoid-crossing phenomenon occurs between the acoustic and optical branches, returning to the classical rattling model. At this time, with the increase of m, ω_{a-max} shows a gradual downward trend in general.

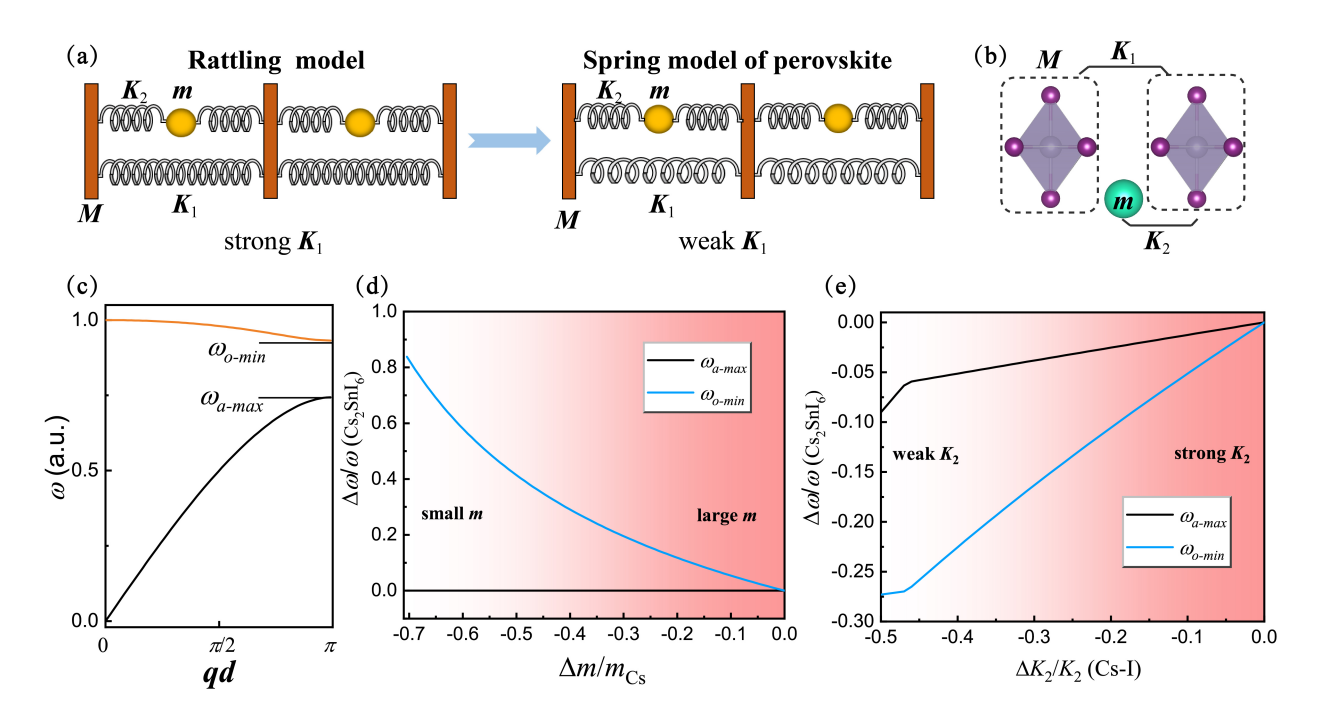


Figure 5: (a) Comparison between rattling model and spring model of $A_2\mathrm{SnI}_6$ perovskites. (b) The structural units in the $A_2\mathrm{SnI}_6$ perovskites coincide with the established spring model. (c) The analytical solution of the spring model corresponds to $\mathrm{Cs}_2\mathrm{SnI}_6$. The variation rate of ω_{a-max} and ω_{o-min} after varying (d) m as well as (e) K_2 on the basis of the $\mathrm{Cs}_2\mathrm{SnI}_6$ spring model parameters.

It is a common phenomenon that phonons of Cs-based halide perovskites are harder than Rb-based halide perovskites. Although the two neighboring octahedra in our chosen

halide chalcogenide system do not share halide atoms, the spring model we have developed is equally applicable to the case of shared halide atoms. In the case of cubic $ASnI_3$ (A=Rb, Cs), as shown in the Fig. S4, CsSnI₃ has harder low-frequency phonons, and after replacing $|\Phi_2(Cs-I)|$ by $|\Phi_2(Rb-I)|$, its low-frequency phonon dispersion is comparable to that of RbSnI₃ as seen in Fig. S4(a, b). However, low-frequency phonons are not sensitive to changes in A^+ mass (Fig. S4(c)). We attribute the phonon dispersion sensitivity to the interaction of A^+ cations and halide anions to that the adjacent octahedral structure interacts weakly in metal halide perovskites. The weak interaction makes the low-frequency phonon branch of the octahedral contribution significantly lower in frequency than the optical branch of the A^+ contribution, thus preventing coupling together to produce avoid-crossing phenomenon. Since the octahedral structure is mainly connected by ionic bonds, the overlap of electron orbitals between adjacent octahedral atoms is weak as seen in the electronic localization function (ELF) shown in Fig. S4(d). From the two vibrational modes of the low-frequency phonons (Fig. S4(e)), it can be seen that the adjacent octahedra rotate independently around their respective centers. The shared halide atoms are not sufficient to significantly enhance the interaction of the neighboring octahedra. The phonon dispersion of double perovskite A_2 AgBiBr₆ (A=Rb, Cs) also shows a similar variation as seen in Fig. S5.

Conclusions

In summary, we comprehensively investigated anomalous heat transport behavior in metal halide perovskites $A_2\mathrm{SnI}_6$ ($A=\mathrm{K}$, Rb, Cs). $\mathrm{Cs}_2\mathrm{SnI}_6$ has the largest total atomic mass but the lowest particlelike thermal conductivity κ_p . The large κ_p of $\mathrm{Cs}_2\mathrm{SnI}_6$ results from strong A-I interaction, bringing about hardened low-frequency phonon branches and weak lattice anharmonicity. The hardening of low-frequency phonon branches further weakens the phonon scattering phase space and leads to large phonon lifetime. The low-frequency phonon branches are not sensitive to the mass of A^+ cations but are sensitive to the interaction between A^+

and I⁻ in $[SnI_6]^{2-}$ octahedra, which is inconsistent with the law given by the classical rattling model. This difference comes from the fact that weak interactions between $[SnI_6]^{2-}$ octahedra fail to satisfy the condition of strong connections between host frames in the rattling model. Using the established spring model, we have successfully explained the variation rule of the phonon dispersion with A^+ cations in A_2SnI_6 perovskites. Our results are important for understanding the heat transport mechanism of perovskites and designing new materials with low thermal conductivity.

Numerical methods

The calculations are implemented using the Vienna Ab Initio simulation package (VASP) based on density functional theory (DFT)³⁰ with the projector augmented wave (PAW) method and revised PBE-GGA exchange—correlation functional for solids (PBEsol).³¹ The cutoff energy of the plane wave is set to 500 eV. The energy convergence value between two consecutive steps is set as 10^{-5} eV when optimizing atomic positions and the maximum Hellmann-Feynman (HF) force acting on each atom is 10^{-3} eV/Å. The calculations of κ_L and other relevant parameters such as phonon relaxation time are carried out by the ShengBTE software 32,33 which operates based on the iterative scheme. The **q**-mesh in the first irreducible Brillouin Zone is set to be $12 \times 12 \times 12$. The Gaussian smearing is set as 0.5. A maximum likelihood estimation method is used to accelerate the calculation of the 4ph scattering rate.³⁴ The sample size is set as 4×10^5 . The recently introduced on-the-fly Machine Learning Potential (FMLP) of VASP is used to accelerate AIMD simulation. The hyperparameters are set to the default values provided by the VASP and the cutoff radius is 8 Å, which allows the root mean square error of the energies to be less than 10^{-4} eV/atom. The supercells of $3\times3\times3$ containing 243 atoms are chosen. The simulation is run for 20 ps with a timestep of 1 fs. The second-order, third-order, and fourth-order IFCs are determined from the AIMD simulation by using the TDEP method.³⁵ The cutoff radius of third-order and fourth-order

IFCs is set as 6 Å and 4 Å respectively.

Conflicts of interest

There are no conflicts to declare.

Acknowledgements

This work is supported by the Natural Science Foundation of China (12304038), the Startup funds of Outstanding Talents of UESTC (A1098531023601205), National Youth Talents Plan of China (G05QNQR049).

References

- (1) Jung, E. H.; Jeon, N. J.; Park, E. Y.; Moon, C. S.; Shin, T. J.; Yang, T.-Y.; Noh, J. H.; Seo, J. Efficient, stable and scalable perovskite solar cells using poly(3-hexylthiophene).

 Nature 2019, 567, 511–515.
- (2) Saliba, M.; Matsui, T.; Domanski, K.; Seo, J.-Y.; Ummadisingu, A.; Zakeeruddin, S. M.; Correa-Baena, J.-P.; Tress, W. R.; Abate, A.; Hagfeldt, A.; Grätzel, M. Incorporation of rubidium cations into perovskite solar cells improves photovoltaic performance. *Science* 2016, 354, 206–209.
- (3) Wang, L.; Zou, X.; Lin, J.; Jiang, J.; Liu, Y.; Liu, X.; Zhao, X.; Liu, Y. F.; Ho, J. C.; Liao, L. Perovskite/black phosphorus/MoS2 photogate reversed photodiodes with ultrahigh light on/ff ratio and fast response. *ACS Nano* **2019**, *13*, 4804–4813.
- (4) Lim, J. W.; Wang, H.; Choi, C. H.; Kwon, H.; Quan, L. N.; Park, W.-T.; Noh, Y.-Y.; Kim, D. H. Self-powered reduced-dimensionality perovskite photodiodes with controlled crystalline phase and improved stability. *Nano Energy* 2019, 57, 761–770.

- (5) Yang, Z.; Deng, Y.; Zhang, X.; Wang, S.; Chen, H.; Yang, S.; Khurgin, J.; Fang, N. X.; Zhang, X.; Ma, R. High-performance single-crystalline perovskite thin-film photodetector. *Adv. Mater.* **2018**, *30*, 1704333.
- (6) Pan, W. et al. Cs2AgBiBr6 single-crystal X-ray detectors with a low detection limit.

 Nat. Photonics 2017, 11, 726–732.
- (7) Xiang, W.; Tress, W. Review on recent progress of all-inorganic metal halide perovskites and solar cells. *Adv. Mater.* **2019**, *31*, 1902851.
- (8) Zeng, X.; Jiang, J.; Niu, G.; Sui, L.; Zhang, Y.; Wang, X.; Liu, X.; Chen, A.; Jin, M.; Yuan, K. Physical insights on the thermoelectric performance of Cs2SnBr6 with ultralow lattice thermal conductivity. J. Phys. Chem. Lett. 2022, 13, 9736–9744.
- (9) Sajjad, M.; Mahmood, Q.; Singh, N.; Larsson, J. A. Ultralow lattice thermal conductivity in double perovskite Cs2PtI6: A promising thermoelectric material. ACS App. Energy Mater. 2020, 3, 11293–11299.
- (10) Bhui, A.; Ghosh, T.; Pal, K.; Singh Rana, K.; Kundu, K.; Soni, A.; Biswas, K. Intrinsically low thermal conductivity in the n-type vacancy-ordered double perovskite Cs2SnI6: Octahedral rotation and anharmonic rattling. Chem. Mater. 2022, 34, 3301–3310.
- (11) Wu, Y.; Ji, J.; Ding, Y.; Yang, J.; Zhou, L. Ultralow lattice thermal conductivity and large glass-like contribution in Cs3Bi2I6Cl3: Rattling atoms and p-band electrons driven dynamic rotation. *Adv. Sci.* **2024**, 2406380.
- (12) Acharyya, P.; Ghosh, T.; Pal, K.; Kundu, K.; Singh Rana, K.; Pandey, J.; Soni, A.; Waghmare, U. V.; Biswas, K. Intrinsically Ultralow Thermal Conductivity in Ruddles-den-Popper 2D Perovskite Cs2PbI2Cl2: Localized Anharmonic Vibrations and Dynamic Octahedral Distortions. J. Am. Chem. Soc 2020, 142, 15595–15603.

- (13) Wu, Y.; Huang, A.; Ji, L.; Ji, J.; Ding, Y.; Zhou, L. Origin of intrinsically low lattice thermal conductivity in solids. *J. Phys. Chem. Lett.* **2024**, 11525–11537.
- (14) Wang, X.; Gao, Z.; Zhu, G.; Ren, J.; Hu, L.; Sun, J.; Ding, X.; Xia, Y.; Li, B. Role of high-order anharmonicity and off-diagonal terms in thermal conductivity: A case study of multiphase CsPbBr3. *Phys. Rev. B* **2023**, *107*, 214308.
- (15) Christensen, M.; Abrahamsen, A. B.; Christensen, N. B.; Juranyi, F.; Andersen, N. H.; Lefmann, K.; Andreasson, J.; Bahl, C. R. H.; Iversen, B. B. Avoided crossing of rattler modes in thermoelectric materials. *Nat. Mater.* 2008, 7, 811–815.
- (16) Dutta, M.; Samanta, M.; Ghosh, T.; Voneshen, D. J.; Biswas, K. Evidence of highly anharmonic soft lattice vibrations in a zintl rattler. Angew. Chem. Int. Ed. 2020, 60, 4259–4265.
- (17) Lin, H.; Tan, G.; Shen, J.; Hao, S.; Wu, L.; Calta, N.; Malliakas, C.; Wang, S.; Uher, C.; Wolverton, C.; Kanatzidis, M. G. Concerted rattling in CsAg5Te3 leading to ultralow thermal conductivity and high thermoelectric performance. *Angew. Chem. Int. Ed.* 2016, 55, 11431–11436.
- (18) Li, J.; Hu, W.; Yang, J. High-throughput screening of rattling-induced ultralow lattice thermal conductivity in semiconductors. J. Am. Chem. Soc. 2022, 144, 4448–4456.
- (19) Varadwaj, P. R. A2AgCrCl6 (A = Li, Na, K, Rb, Cs) halide double perovskites: a transition metal-based semiconducting material series with appreciable optical characteristics. *Phys. Chem. Chem. Phys.* **2020**, *22*, 24337–24350.
- (20) Mahmood, Q.; Zelai, T.; Hassan, M.; Nazir, G.; Albalawi, H.; Sfina, N.; Kattan, N. A.; Hakamy, A.; Mera, A.; Amin, M. A. Study of lead-free double perovskites X2AgBiI6 (X = K, Rb, Cs) for solar cells and thermoelectric applications. J. Mater. Res. Technol. 2023, 22, 913–922.

- (21) Cheng, R.; Zeng, Z.; Wang, C.; Ouyang, N.; Chen, Y. Impact of strain-insensitive low-frequency phonon modes on lattice thermal transport in A2XB6-type perovskites. *Phys. Rev. B* **2024**, *109*, 054305.
- (22) Ayyaz, A.; Murtaza, G.; Usman, A.; Sfina, N.; Alshomrany, A. S.; Younus, S.; Saleem, S.; tul Aysha, U. Evaluation of physical properties of A2ScCuCl6 (A=K, Rb, and Cs) double perovskites via DFT framework. *J. Inorg. Organomet. P.* **2024**, *34*, 3560–3575.
- (23) Thakur, S.; Giri, A. Origin of ultralow thermal conductivity in metal halide perovskites. ACS Appl. Mater. 2023, 15, 26755–26765.
- (24) Di Lucente, E.; Simoncelli, M.; Marzari, N. Crossover from Boltzmann to Wigner thermal transport in thermoelectric skutterudites. *Phys. Rev. Res.* **2023**, *5*.
- (25) Ji, L.; Huang, A.; Huo, Y.; Ding, Y.-m.; Zeng, S.; Wu, Y.; Zhou, L. Influence of four-phonon scattering and wavelike phonon tunneling effects on the thermal transport properties of TlBiSe2. *Phys. Rev. B* **2024**, *109*, 214307.
- (26) Tong, Z.; Zhang, Y.; Pecchia, A.; Yam, C.; Zhou, L.; Dumitrică, T.; Frauenheim, T. Predicting the lattice thermal conductivity in nitride perovskite LaWN3 from ab initio lattice dynamics. *Adv. Sci.* **2023**, *10*, 2205934.
- (27) Wu, Y.; Chen, Y.; Fang, Z.; Ding, Y.; Li, Q.; Xue, K.; Shao, H.; Zhang, H.; Zhou, L. Ultralow lattice thermal transport and considerable wave-like phonon tunneling in chalcogenide perovskite BaZrS3. J. Phys. Chem. Lett. 2023, 14, 11465–11473.
- (28) Zhang, J.; Ishikawa, D.; Koza, M. M.; Nishibori, E.; Song, L.; Baron, A. Q. R.; Iversen, B. B. Dynamic lone pair expression as chemical bonding origin of giant phonon anharmonicity in thermoelectric InTe. Angew. Chem. Int. Ed. 2023, 135, e202218458.

- (29) Dronskowski, R.; Bloechl, P. E. Crystal orbital Hamilton populations (COHP): energy-resolved visualization of chemical bonding in solids based on density-functional calculations. J. Phys. Chem. 1993, 97, 8617–8624.
- (30) Kresse, G.; Furthmuller, J. Efficient iterative schemes for ab initio total-energy calculations using a plane-wave basis set. *Phys. Rev. B* **1996**, *54*, 11169–11186.
- (31) Perdew, J. P.; Ruzsinszky, A.; Csonka, G. I.; Vydrov, O. A.; Scuseria, G. E.; Constantin, L. A.; Zhou, X.; Burke, K. Restoring the density-gradient expansion for exchange in solids and surfaces. *Phys. Rev. Lett.* **2008**, *100*, 136406.
- (32) Li, W.; Carrete, J.; Katcho, N. A.; Mingo, N. ShengBTE: A solver of the Boltzmann transport equation for phonons. *Comput. Phys. Commun.* **2014**, *185*, 1747–1758.
- (33) Han, Z.; Yang, X.; Li, W.; Feng, T.; Ruan, X. FourPhonon: An extension module to ShengBTE for computing four-phonon scattering rates and thermal conductivity. *Comput. Phys. Commun.* **2022**, *270*, 108179.
- (34) Guo, Z.; Han, Z.; Feng, D.; Lin, G.; Ruan, X. Sampling-accelerated prediction of phonon scattering rates for converged thermal conductivity and radiative properties. *npj Comput. Mater.* **2024**, *10*.
- (35) Hellman, O.; Abrikosov, I. A. Temperature-dependent effective third-order interatomic force constants from first principles. *Phys. Rev. B* **2013**, *88*, 144301.